

CFD analysis of natural convection cooling of the in-vessel components during a shutdown of the EU DEMO fusion reactor

Original

CFD analysis of natural convection cooling of the in-vessel components during a shutdown of the EU DEMO fusion reactor / Zappatore, Andrea; Froio, Antonio; Spagnuolo, Gandolfo Alessandro; Zanino, Roberto. - In: FUSION ENGINEERING AND DESIGN. - ISSN 0920-3796. - STAMPA. - 165:(2021), p. 112252. [10.1016/j.fusengdes.2021.112252]

Availability:

This version is available at: 11583/2869430 since: 2021-02-05T19:15:52Z

Publisher:

Elsevier

Published

DOI:10.1016/j.fusengdes.2021.112252

Terms of use:

This article is made available under terms and conditions as specified in the corresponding bibliographic description in the repository

Publisher copyright

Elsevier postprint/Author's Accepted Manuscript

© 2021. This manuscript version is made available under the CC-BY-NC-ND 4.0 license
<http://creativecommons.org/licenses/by-nc-nd/4.0/>. The final authenticated version is available online at:
<http://dx.doi.org/10.1016/j.fusengdes.2021.112252>

(Article begins on next page)

CFD analysis of natural convection cooling of the in-vessel components during a shutdown of the EU DEMO fusion reactor

Andrea Zappatore¹, Antonio Froio^{1,*}, Gandolfo Alessandro Spagnuolo² and Roberto Zanino¹

¹*NEMO group, Dipartimento Energia, Politecnico di Torino, 10129 Torino, Italy*
²*PPPT Department, EUROfusion Consortium, 85748 Garching bei München, Germany*

In view of the large neutron fluence expected in a fusion power plant, the maintenance of the in-vessel components (IVC) must be carried out using Remote Handling (RH); however, before the RH robots can intervene, the temperature of the IVCs must be reduced, so a cooldown phase is required after the reactor shutdown before maintenance activities can start. In the EU DEMO two options are being investigated to cool down the Breeding Blanket (BB) structures before maintenance, namely introducing fans to pump air in forced convection in the plasma chamber (after opening the Vacuum Vessel), or letting the air at room temperature cool down the structures by natural convection; if the required downtime is acceptable, the second option is clearly preferred, as it would reduce the cost and complexity of the system. This work analyses the natural convection option via a 3D transient Computational Fluid-Dynamics (CFD) conjugate heat transfer model, to evaluate the required time to cool down the BB.

Keywords: DEMO, in-vessel component, natural convection, conjugate heat transfer, CFD, remote handling

1. Introduction

The EU DEMO, being developed by the EUROfusion Consortium, is the tokamak fusion reactor aiming to demonstrate the production of electricity (300-500 MW) from fusion power plants in Europe [1]. As the first European device to include a full-scale Breeding Blanket (BB), it will operate as a Component Test Facility for the BB [2], which will then be replaced not only if extraordinary maintenance is needed but also to test different BB concepts, and whenever the BB set will reach the end of life. As the BB first wall directly faces the plasma, the BB will be subject to the largest total neutron fluence and will be activated, requiring a Remote Handling (RH) system to operate on it for maintenance.

Current RH system designs in EUROfusion foresee a temperature limit to operate the RH of 100-150 °C [3], whereas the operating temperature window of the BB is 300÷550 °C during normal operation; in addition, the BB will heat up also after the shutdown, in view of the decay heat generated therein (~1-2 % of the power released during the flat-top immediately after the shutdown [4]). Consequently, after the reactor shutdown, the BB must be cooled down before the first segment can be removed; the BB transporter will extract all BB segments from the upper port [5], see Fig. 1, from which also the BB coolant inlet and outlet pipes are routed [2]. To maximize the plant availability, the downtime caused by the maintenance should be minimized, and consequently, also the time needed to cool down the segments play a role in the plant performance. If an active cooling system is employed, this time can be reduced, however introducing

52 further complexity and cost in the plant; on the other hand, 53 if the Vacuum Vessel (VV) is opened, the BB segments 54 will be passively cooled in natural convection by the air 55 entering at room temperature from the lower port, see Fig. 56 1.

57 In the present work, the natural convection cooling 58 strategy is assessed, in order to find the time needed to 59 meet the RH requirement after the reactor has been shut 60 down. To this aim, a 3D transient CFD conjugate heat 61 transfer (CHT) model was developed and applied using 62 the software STAR-CCM+ v. 2019.3 [6]. To the best of 63 the authors' knowledge, this is the first time that a 3D 64 transient thermal-hydraulic model is employed to analyse 65 the cooldown transient of the BB during reactor 66 shutdown; indeed, most of past efforts have been put 67 either in estimating the shutdown dose rate (see e.g. 68 [7][8]), or on pure thermal analyses including radiative 69 and conductive heat transfer only (see e.g. [9][10]). More 70 recently, a CFD analysis of the natural circulation of the 71 helium coolant in the DEMO cryostat following a Loss- 72 of-Coolant Accident has been carried out [11]; however, 73 the work was focused on accidental condition and carried 74 out by means of steady-state simulations only.

75

2. The 3D CFD model

2.1 Model equations

78 The 3D CFD model implemented in STAR-CCM+ 79 enforces the fundamental conservation laws of mass, 80 momentum and energy [12], in both the fluid and solid 81 domains.

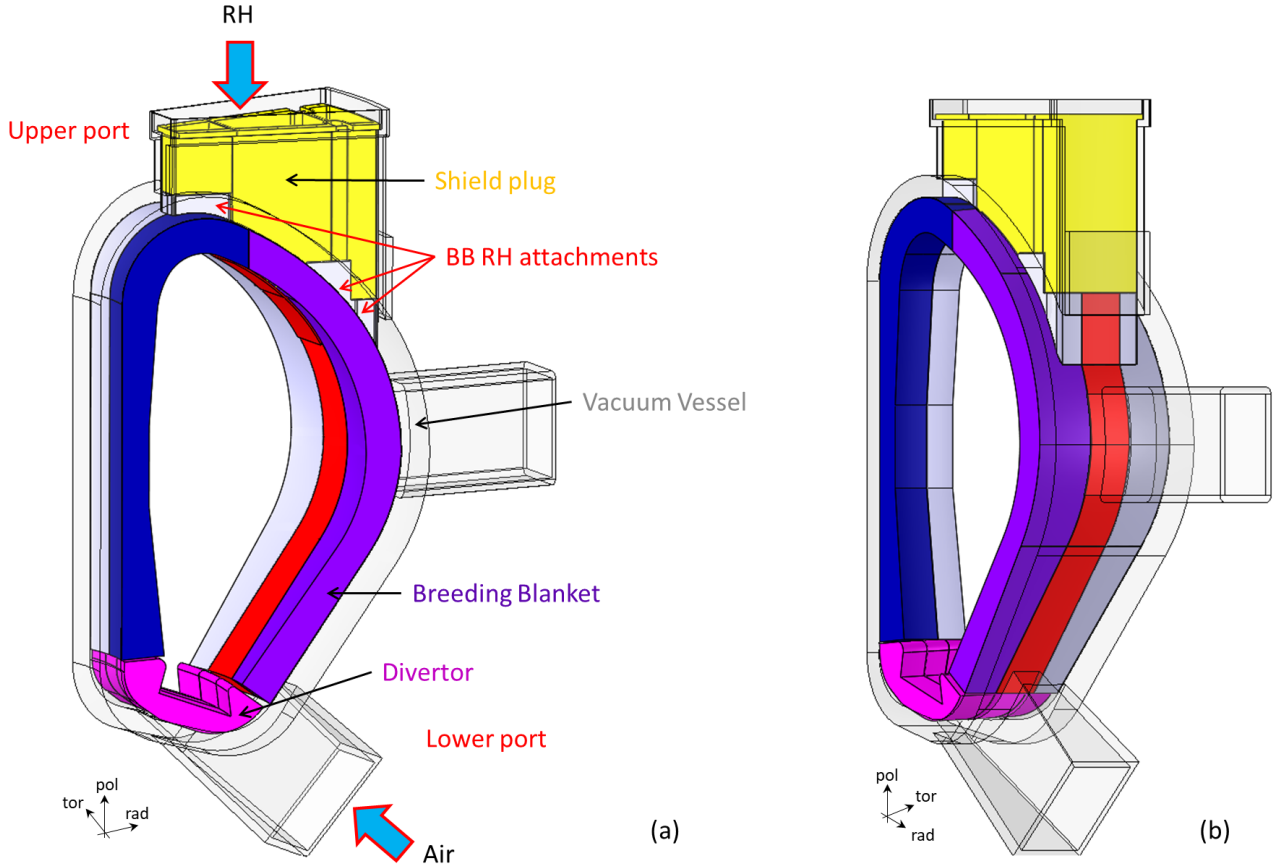


Fig. 1. View of one sector of the EU DEMO, showing the internals (BB, divertor, shield plug), the upper port where the RH operates and the lower port where air enters the VV. The BB attachments for RH operation are also shown.

Both the solid and the fluid are assumed to have constant thermophysical properties (density ρ , specific heat c , dynamic viscosity μ , thermal conductivity k); however, as the driver of fluid motion in natural convection is buoyancy (driven in turn by the density differences), the body force term in the fluid momentum equation \mathbf{f}_b is computed via the Boussineq approximation as

$$\mathbf{f}_b = \rho \mathbf{g} \beta (T_{ref} - T) \quad (1)$$

where \mathbf{g} is the gravity acceleration, $\beta = 1/T_{ref}$ is the thermal expansion coefficient of the fluid (assumed constant), $T_{ref} = 300$ K is the reference temperature and T is the local fluid temperature.

The conductive heat flux \mathbf{q}'' (in both solid and fluid) is computed via Fourier's law of conduction

$$\mathbf{q}'' = -k \nabla T \quad (2)$$

Note that no volumetric heat source q''' is present in the fluid energy equation, whereas its value in the solid domain is a known term, whose value is reported in section 2.4 below.

Under these assumptions, for the fluid domain the three above-mentioned laws correspond to the set of incompressible Navier-Stokes equations:

$$\nabla \cdot \mathbf{v} = 0 \quad (3)$$

$$\frac{\partial(\mathbf{v})}{\partial t} + (\mathbf{v} \cdot \nabla) \mathbf{v} = -\frac{1}{\rho} \nabla p + \nu \nabla^2 \mathbf{v} + \frac{1}{\rho} \mathbf{f}_b \quad (4)$$

$$\rho \frac{\partial E}{\partial t} + \rho (\mathbf{v} \cdot \nabla) E =$$

$$= -(\mathbf{v} \cdot \nabla) p + \nabla \cdot (\mathbf{v} \cdot \boldsymbol{\sigma}) + \mathbf{f}_b \cdot \mathbf{v} + k \nabla^2 T \quad (5)$$

where t is the time, $\nu = \mu/\rho$ is the kinematic viscosity, p is the pressure, $E = e + \frac{1}{2} |\mathbf{v}|^2$ is the total energy per unit mass, e is the specific internal energy and $\boldsymbol{\sigma}$ is the stress tensor.

Concerning the solid domain, since it has zero velocity (and its mass is not changing), only the energy conservation equation is required. Under the assumptions above, and recalling that the internal energy variation dE can be expressed in terms of temperature variation (via the specific heat definition $dE = c dT$), it takes the form

$$\rho c \frac{\partial T}{\partial t} = k \nabla^2 T + q''' \quad (6)$$

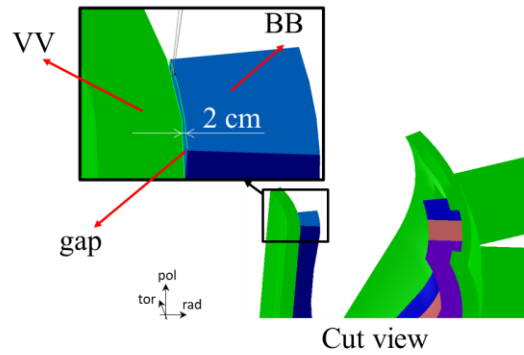
2.2 Geometry

The reference geometry assumed in this work is taken from the EU DEMO 2017 baseline [13], [14]; as BB concept the Helium-Cooled Pebble Bed [15] (HCPB) is assumed. A possible application of the present model to the Water-Cooled Lithium Lead [16] (WCLL) concept

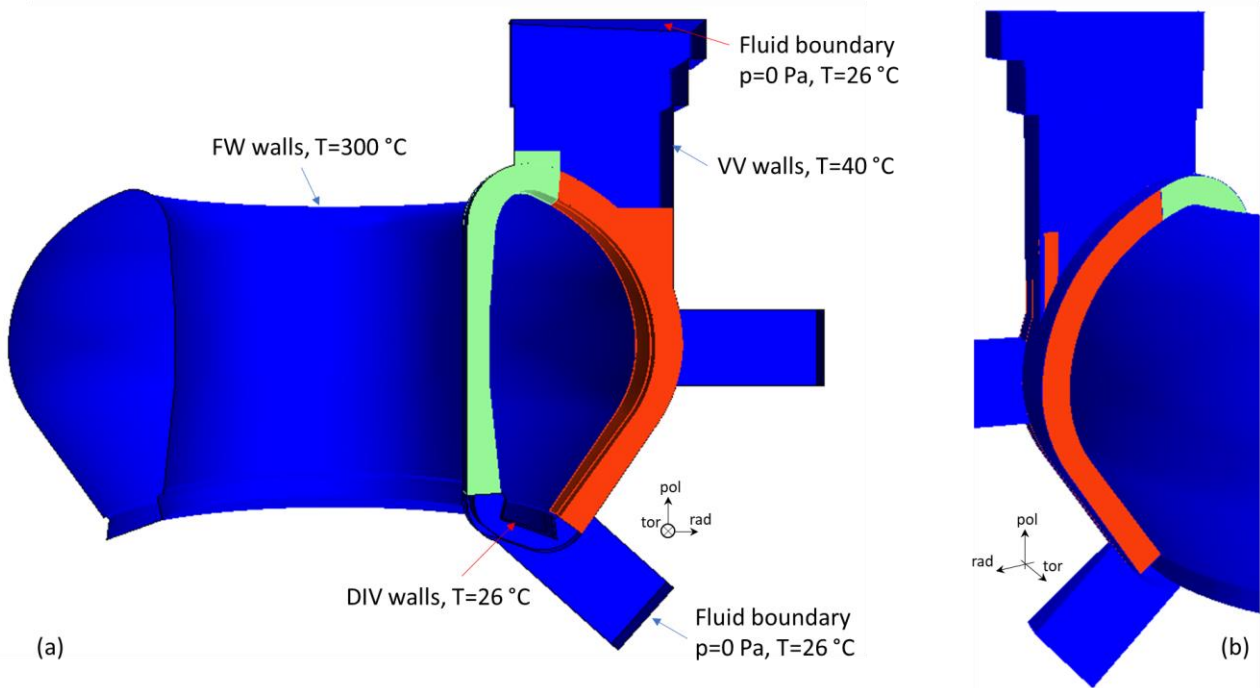
1 would be straightforward since the only changes in the
 2 model would be the different material properties and heat
 3 load, which would affect significantly the transient timing
 4 but not the model, solvers, and meshing strategy described
 5 here.

6 The air entering from the lower port will flow in the
 7 2 cm gaps between two adjacent BB segments and
 8 between the BB and the VV, see Fig. 2; this dimension is
 9 extremely small when compared to the tens of meters of
 10 the plasma chamber, so detailed modelling is included
 11 only for the sector under maintenance (as maintenance is
 12 assumed to be performed one sector at a time [17]). This
 13 choice is justified considering that the BB sectors *not*
 14 under maintenance will be actively kept at $\sim 300\text{ }^\circ\text{C}$ using
 15 the helium cooling system [17]; moreover, the shield plug
 16 will be removed only from the upper port of the sector
 17 under maintenance, so the flow in the gaps in the non-
 18 maintained sectors can be considered negligible. In view
 19 of this assumption, the domain boundary in the non-

20 maintained sectors is the envelope of the First Wall (FW)
 21 and divertor plasma-facing surfaces, see Fig. 3.



22
 23
 24
 25
 26 Fig. 2. Cut view of an EU DEMO sector, showing in the inset the gap between BB and VV.



27
 28
 29
 30 Fig. 3. (a) Computational domain including the BB sector and VV considered for the present analysis. The IB and OB segments
 31 are coloured in light green and red, respectively. The solid and fluid boundary conditions are also shown. (b) Rear view of the
 32 computational domain.

33
 34 Finally, just as the BB and VV geometries, also the
 35 boundary conditions and thermal driver (see below) are
 36 symmetric with respect to a vertical plane which cuts in
 37 half the maintained sector; therefore, only half of the
 38 tokamak is considered here, cutting it with a vertical plane
 39 passing through the vertical midplane of the sector
 40 undergoing maintenance; note that this vertical midplane
 41 cuts in half the central outboard (OB) segment and the gap
 42 between the two inboard (IB) segments, i.e. it belongs to

43 the solid domain on the OB and to the fluid domain on the
 44 IB. The computational domain is reported in Fig. 3, where
 45 the OB and IB segments are coloured in red and light
 46 green, respectively.

47 The computational domain includes a fluid region
 48 (lower port, equatorial port, upper port and VV) and the
 49 solid structures of the inboard and outboard segments of
 50 one BB sector.

51

2.3 Boundary and initial conditions

The upper and lower ports are assumed to be open and in contact with the environment of the tokamak building, while the equatorial port is assumed to be closed; to simulate environmental conditions, the top surface of the upper port and the bottom surface of the lower port are at fixed pressure (0 Pa gauge) and temperature (assuming ambient conditions, i.e. 26 °C). The air could then, in principle, enter (and exit) from both the upper and the lower port; however, due to stack effect [18], it is expected to flow upwards, and then enter from the lower port and exit from the upper port. On the symmetry surfaces, the normal velocity and the normal gradient of all the other variables are zero. The envelope of the FW, see section 2.2, is set at a constant and uniform temperature equal to 300 °C, since all the other non-maintained sectors are assumed to be kept at that temperature. The same assumption holds for the VV and for the divertor, whose surfaces are then set at 40 °C [19], 20 [20] and 26 °C [19], respectively; radiative heat transfer towards these low-temperature surfaces is conservatively neglected. The boundary conditions are summarized in Fig. 3(a).

As initial conditions, the working fluid (air, modelled as ideal gas) is assumed to be stagnant (zero velocity) and at a pressure of 0 Pa gauge; both the solid and the fluid domain are assumed at 300 °C. This assumption stems from having a relatively long time (1 month, see section 2.4 below), during which air is let in and all the BB surfaces (as well as internals) are actively kept at 300 °C.

31

2.4 Thermal driver

The thermal driver in the transient is represented by the decay heat in the BB. It has been fitted to a continuous function from the data available in [21], see Fig. 4. The best fit equation is

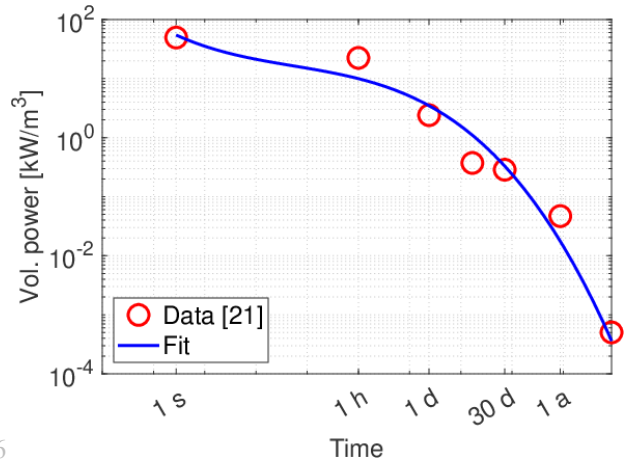
$$\log_{10} \frac{q'''}{q_0} = a(\log_{10} t)^3 + b(\log_{10} t)^2 + c \log_{10} t + d \quad (7)$$

where t is the time after reactor shutdown in seconds, $q_0 = 256.7 \text{ W/m}^3$ for the IB segments and $q_0 = 216.5 \text{ W/m}^3$ for the OB segments; the fit constants are $a = -0.015713$, $b = 0.108177$, $c = -0.393218$ and $d = 2.28004$.

The start time of the transient is 1 month after shutdown, to take into account the time needed to remove the shield plug and cut the coolant pipes in the upper port, to allow RH operation therein [19]. The heat is assumed to be deposited uniformly in all the OB and IB segments; however, the BB segments in the sectors not undergoing maintenance will have the coolant pipes in place and the cooling system active, which, being designed to withstand the nominal load, will maintain the solid temperature

51 fixed at ~300 °C as discussed above. In the maintained 52 sector, instead, the cooling system will not be active 53 anymore as the coolant pipes will be cut as mentioned 54 above.

55



56

57

58 Fig. 4. Time evolution of the decay heat, averaged
59 between inboard and outboard; the circles represent the
60 data taken from [21].

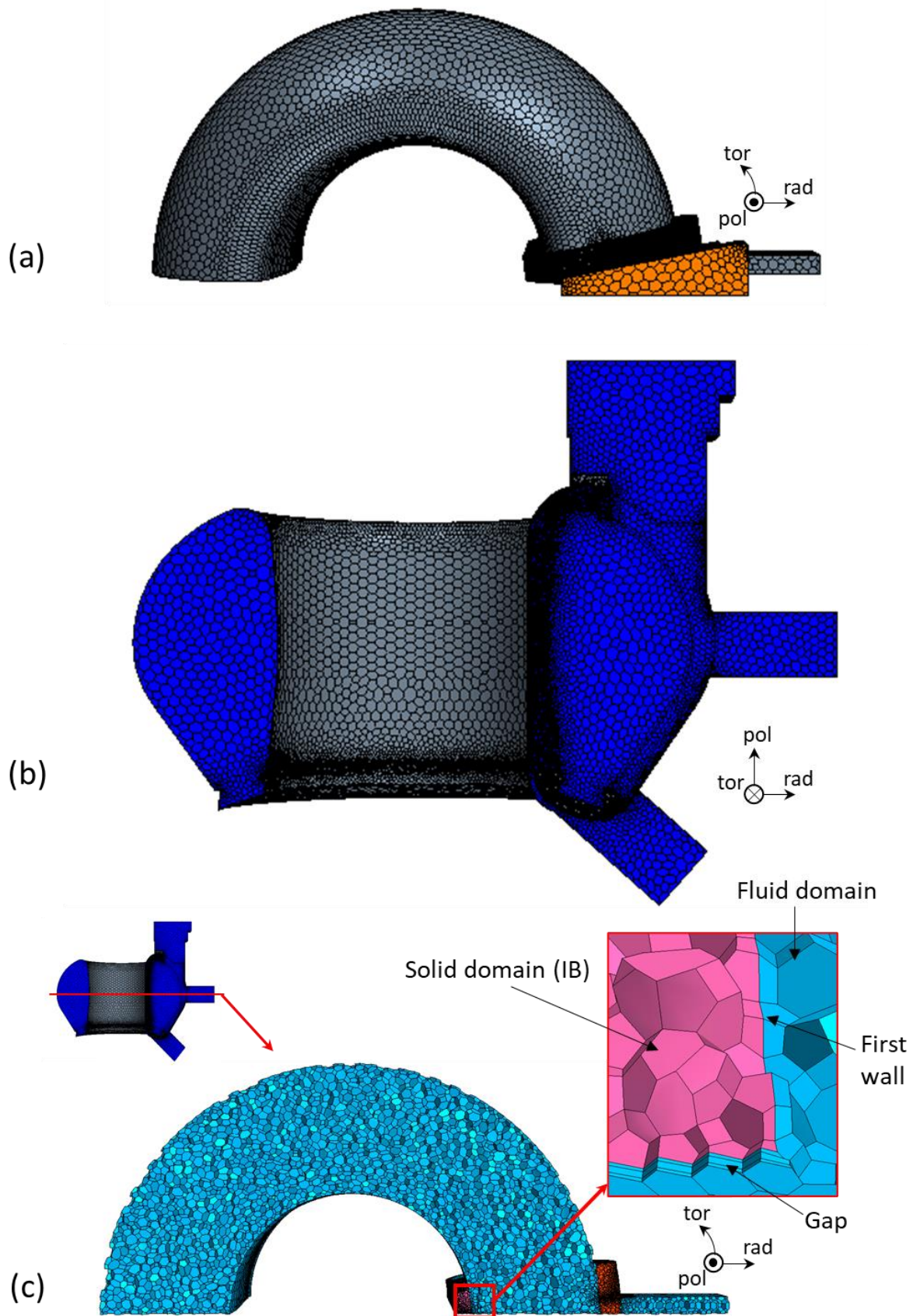
61

3. Space and time scales affecting mesh and solution strategy

The problem at hand is a classical multiscale problem, considering both the space and the time domain. Indeed, as mentioned in section 2.2, the regions where most of the flow will occur are the 2 cm thick gaps at the top and bottom of the segments, where the whole mass flow rate will be forced to flow, and the largest speeds (and velocity gradients) are expected; on the other hand, the vertical dimension of the segments is ~10 m and the domain length in the toroidal direction is ~30 m. Considering also that in the plasma chamber region, and in particular far from the sector undergoing maintenance, the velocities are expected to be much lower than in the gaps, a strongly non-uniform mesh is generated in the fluid region.

More in detail, an unstructured, conformal, polyhedral mesh is used in the solid and fluid regions, except for the gaps, where a structured, conformal, hexahedral mesh is adopted, to resolve the fluid flow without increasing dramatically the cell count (the grid independence study for the mesh in the gap region is reported in the Appendix A). A detailed view of the mesh adopted in this work is available in Fig. 5; the overall cell count is ~4×10⁵ cells, ~90 % of which are in the sector undergoing maintenance.

86



1
2
3 Fig. 5. Top view (a), poloidal cross-section and front view (b) and horizontal cross-section (c) of the mesh adopted for this
4 work. The surfaces are coloured according to the type of fluid boundary condition: blue = symmetry plane, grey = wall and
5 orange = pressure outlet. In (c) a zoom shows the layered mesh in the fluid domain in the gaps between adjacent segments and
6 a much coarser mesh in the remaining solid and fluid regions.

Concerning the time scales,

- the advective time scale can be estimated as L_f/v (where $L_f \sim 9$ m is the height of the chamber and $v \sim 6$ m/s¹), yielding ~ 1 s,
- the convection time scale is $\sim 10^5$ s; it can be estimated as $\rho c V / (HTC \cdot A)$ where V is the solid volume (see Appendix B), respectively, $HTC \sim 4$ W/(m² K) (estimated in Appendix A) is the heat transfer coefficient and A is the heat transfer area,
- the conduction time scale is also $\sim 10^5$ s and can be estimated computed as L_s^2/α , where $L_s = V/A \sim 2$ m is the solid characteristic length and $\alpha = k/\rho c$ is the solid thermal diffusivity (see Appendix B).

As a consequence, the fluid solver in principle requires a much shorter time step with respect to the solid solver, i.e. if the two solver are run in a fully-coupled fashion, the solid solver is called unnecessarily often to keep the pace of the fluid solver (which is the bottleneck due to the

shorter time scale and to the larger complexity of the model, see section 2.1 above).

To speed up the solution of the transient CHT problem, we adopt a partially decoupled approach: the fluid solver works with a time step $\Delta t_{fluid} = 0.2$ s and the solid solver with a time step $\Delta t_{solid} = 1$ s. The two solvers proceed in series, synchronising them periodically (every Δt_{solid}), i.e. exchanging the required information according to the scheme in Fig. 6: at each solid time step, the solid solver provides the fluid solver with the solid (surface) temperature; the fluid solver, after 5 time steps, provides back the solid solver with the fluid temperature and heat transfer coefficient. These operations are automatically repeated by the software until the transient is finished. Considering also that the solution of the heat diffusion problem is very fast (requiring usually one iteration per time step to converge), thanks to this approach, the time required for the simulation is nearly identical to that required by a pure fluid simulation.

The space and time convergence studies are reported in the 0.

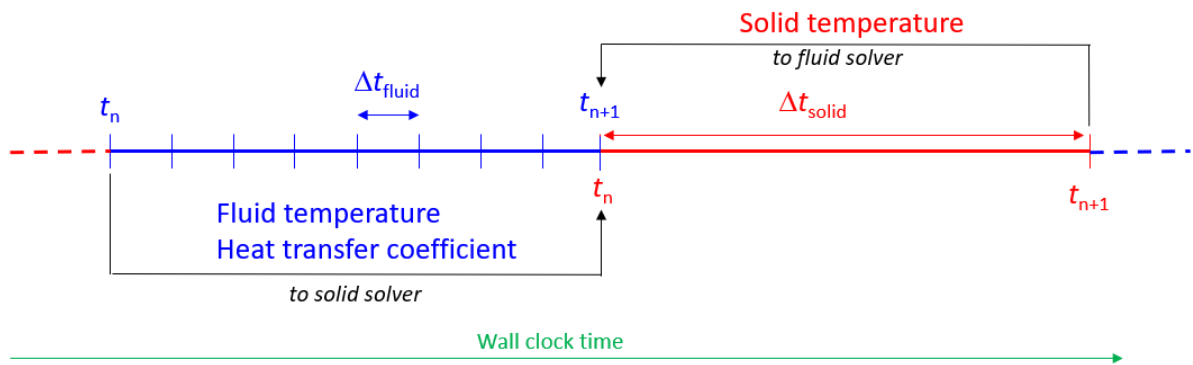


Fig. 6. Coupling strategy between fluid and solid solvers; the exchanged information is also reported. Note that the wall clock time (green arrow) needed to solve each Δt is not to scale.

43

44

45

46

47

48 4. Models and solvers

49 In order to choose the most appropriate models and
50 solvers, the flow regime is assessed estimating the
51 Rayleigh number Ra according to

$$Ra = \frac{g\beta(T_s - T_\infty)\delta^3}{\nu\alpha} \quad (8)$$

52 which is valid when the solid surface temperature T_s is
53 imposed; here T_∞ is the fluid bulk temperature and δ is
54 the gap thickness. Since the temperature difference at the
55 numerator will decrease with time, Ra is computed at the
56 beginning of the transient to have an upper bound. In our
57 case, considering $T_s = 300$ °C and $T_\infty = 26$ °C, $Ra \cong 3 \cdot$
58 10^5 ; as $Ra < 10^9$, the flow regime will be laminar [22].
59 This assumption has been verified a posteriori, computing

60 Ra from the simulation results: indeed, in the entire
61 domain, and during the entire transient, the computer Ra
62 is always $< 2 \cdot 10^5$.

63 A coupled solver for the set of laminar Navier-Stokes
64 equations plus the energy conservation equation is used,
65 according to [23], as the momentum equation driver is the
66 buoyancy term, which depends on the temperature field;
67 as $\beta(T_s - T_\infty) < 1$, the Boussinesq approximation is used
68 to treat the temperature dependency of the density [22],
69 see also section 2.1 above.

70 These choices have been validated against a simple
71 case (see Appendix A). The material properties used in

¹ The velocity has been estimated from the stack effect relation $v = C \sqrt{2gh \frac{T_i - T_o}{T_i}}$ [18], where C is the discharge coefficient, g is the gravity acceleration, h is the stack

height, T_i and T_o are the warm and cold temperatures. In the case at hand, $C = 0.65$, $h = 9$ m, $T_i = 300$ °C and $T_o = 26$ °C.

1 this work are reported in the Appendix B. The simulation
2 file is available in [24].

3

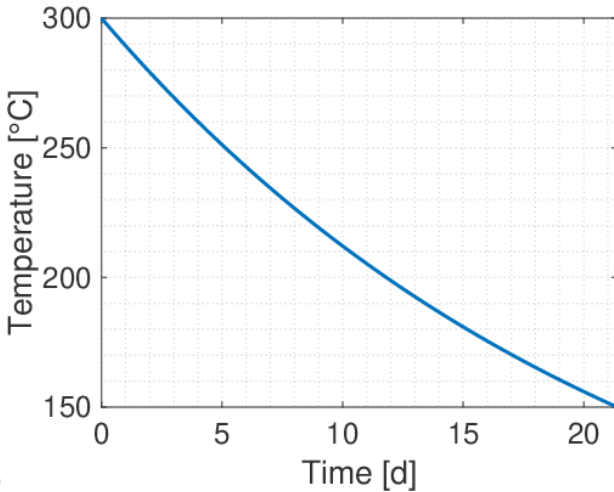
4 5. Results

5 A simple lumped (0D) analysis, see the equation
6 below, estimates that ~21 days are needed to reach 150 °C
7 on average in the segments;

$$\rho c_p V \frac{dT}{dt} = q''' V + h A_w (T_f - T) \quad (9)$$

8 In (9), ρ and c_p are the *average* density and specific
9 heat of the segments, respectively, see Appendix B, V is
10 the total volume of the segments, T is the average
11 temperature of the segments, q''' is the volumetric heat
12 generation, see section 2.4, h is the heat transfer
13 coefficient computed according to (12), A_w is the wetted
14 surface (to be consistent with (8), only the surfaces
15 exposed to the gaps have been considered, leading to
16 $A_w = 88 \text{ m}^2$) and T_f is the fluid temperature, assumed
17 constant and equal to 26 °C. The temperature evolution,
18 as computed with the lumped model, is reported in Fig. 7.

19



20

21

22 Fig. 7. Time evolution of the temperature in the BB
23 segments, as computed with the lumped (0D) model.

24

25 This 0D analysis is however only a rough and
26 especially non-conservative estimate of the expected
27 transient duration, which will necessarily be longer as 1)
28 the temperature of interest is local rather than average and
29 2) the surrounding walls are kept at high temperature
30 (300 °C), which will also heat up the fluid.

81

31 Fig. 8 reports the temperature field on the symmetry
32 plane of the maintained sector, which cuts the gap
33 between the two IB segments and the central OB segment,
34 at different times throughout the transient. As fresh air
35 enters the VV mainly from the lower port (due to natural
36 circulation, see also the discussion below), the BB
37 segments tend to cool down from the bottom part, which
38 is non-optimal as the RH system will intervene from the
39 top, that remains hotter for the entire transient duration.
40 Moreover, the figure shows that heating of the BB
41 segments, both IB and OB, because of the decay heat,
42 lasts ~6 hours only. After that, the bottom part reaches an
43 acceptable temperature after ~2 days, whereas the top of
44 both segments cools down in a much longer time; this
45 result is driven by the long conduction time scale
46 identified above (~ 10^5 s, i.e. ~2 d), as well as by the
47 complex path the fresh air has to follow to reach it.

48 Fig. 9 reports the evolution of the maximum and
49 average solid and fluid temperatures, as well as the
50 temperature evolution as computed with the 0D model; in
51 the 3D model, the average solid temperature is obtained
52 as the volume-averaged value in all the BB segments
53 (both IB and OB), and the average fluid temperature is
54 obtained as the volume-averaged value in the entire fluid
55 domain. The initial increase phase is indeed negligible
56 (lasting ~6 h and reaching a maximum value ~301 °C),
57 due to the low value of the decay heat. The maximum
58 temperature decreases then with an exponential trend,
59 reaching the RH system threshold after ~15 d on the OB
60 and ~85 d on the IB. Note that, in order to let the
61 temperature decrease by few °C as the solid temperature
62 gets closer to that of the fluid, it takes several weeks, i.e.
63 65 days are needed to go from 170 °C to 150 °C
64 maximum temperature at the IB. As can be seen from Fig.
65 9(b), the asymptotic temperature to which the solid tends
66 is ~100 °C, i.e. the average fluid temperature. The key
67 aspect is that such asymptotic behavior of the OB
68 temperature starts after the target temperature has been
69 reached and thus does not affect the RH operation start
70 time, whereas for the IB it starts when the maximum
71 temperature is ~20 °C above the threshold, causing the
72 transient time to increase significantly. A possible
73 mitigation action could then be to slightly enlarge the
74 operation window of the RH system: for instance, an
75 increase of 10 °C (from 150 °C to 160 °C) would reduce
76 the cooldown time to ~30 d, whereas increasing to 170 °C
77 would allow operating after 20 d. Nevertheless, as the OB
78 segments will be removed first [5], RH operations may
79 start when the OB is sufficiently cool, leaving the IB more
80 time to cool down.

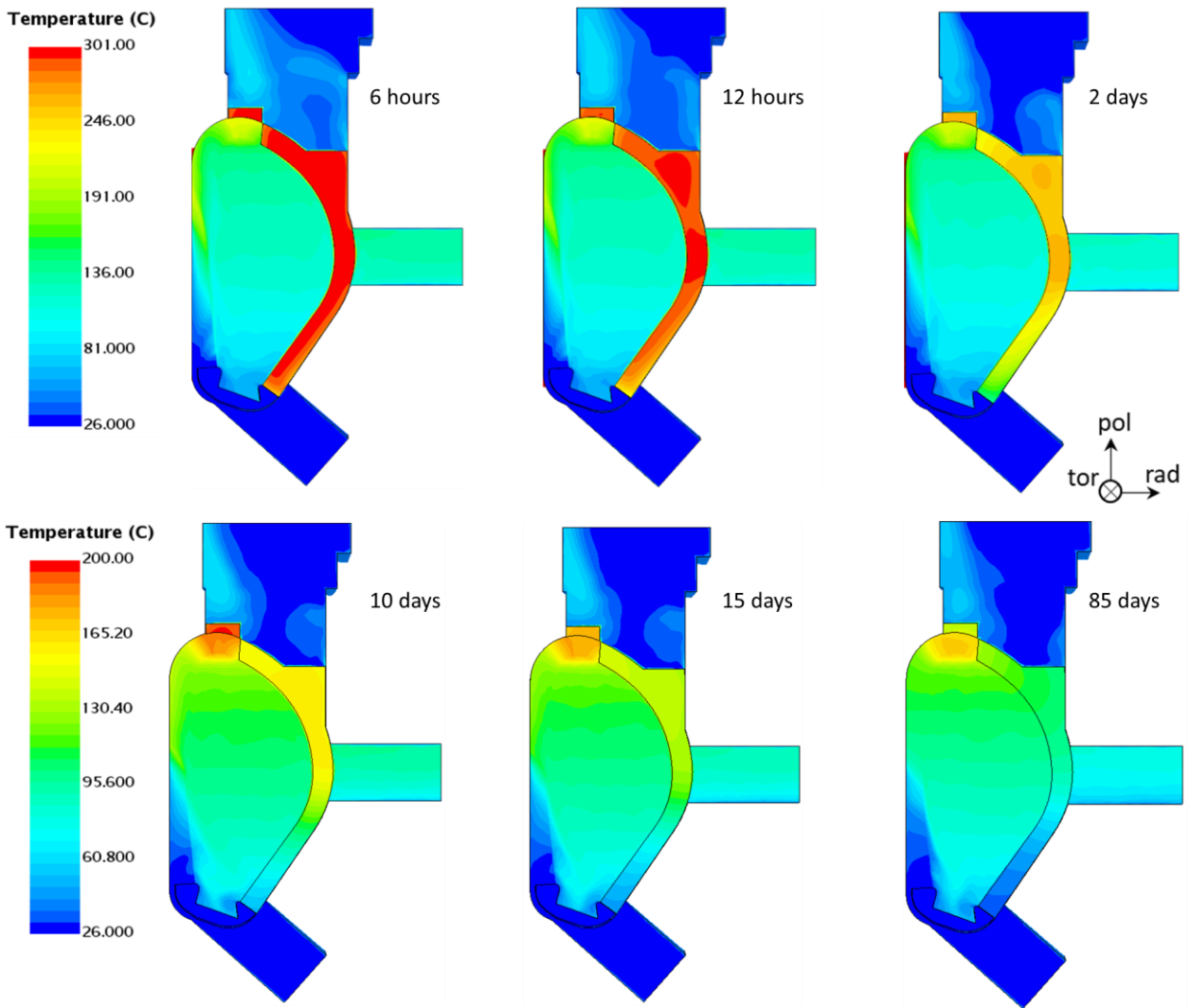


Fig. 8. Temperature field on the symmetry plane of the maintained sector at different times; note that on the second row of the figure, the temperature scale is different, to better appreciate the temperature distribution.

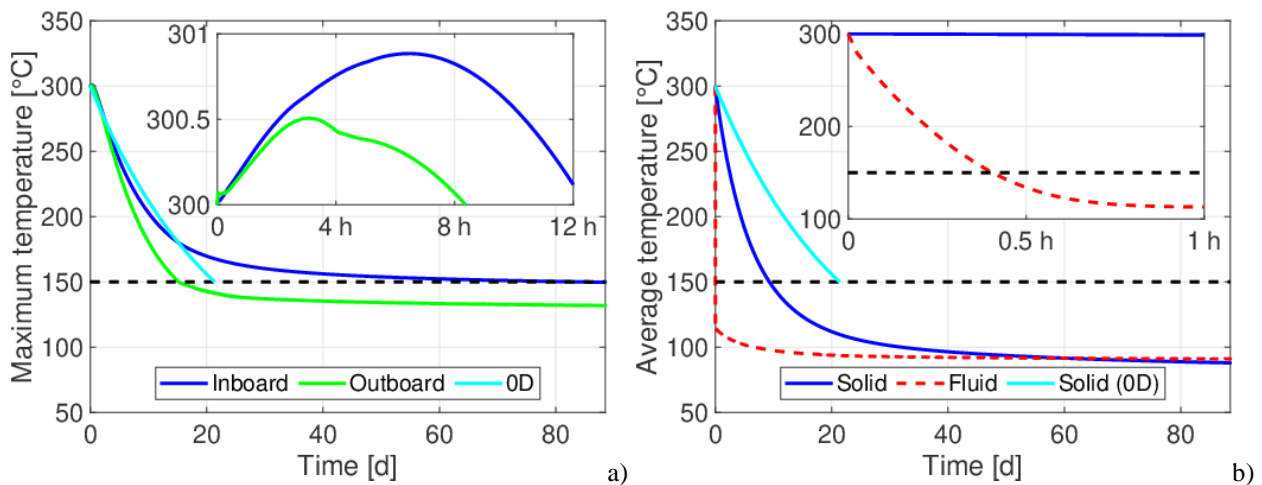


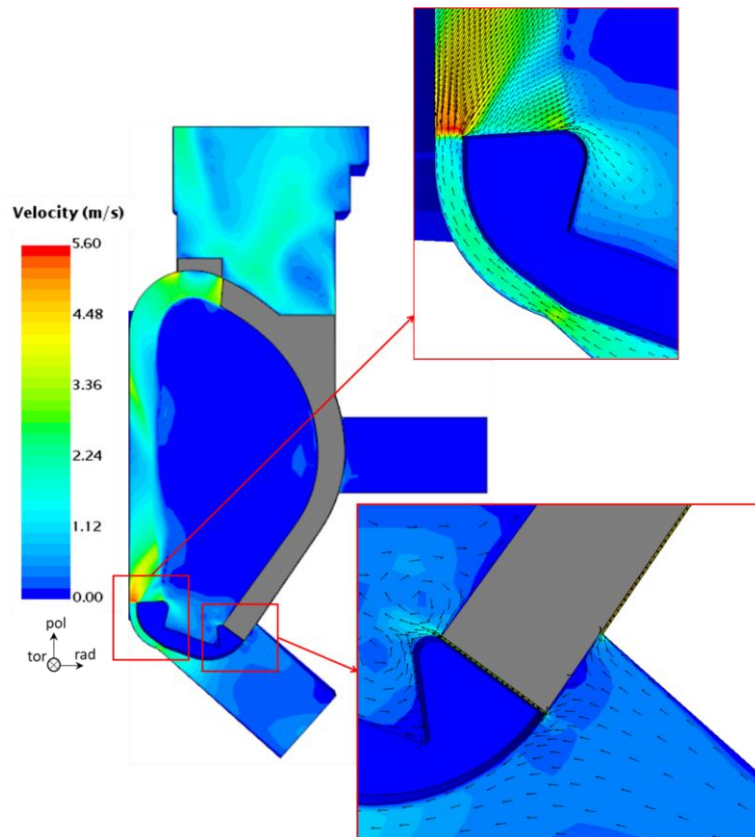
Fig. 9. Evolution of (a) maximum solid temperature and (b) average temperature in the solid and fluid domains; the solid temperature evolution computed with the 0D model is also reported. The dashed black line represents the 150 °C threshold. The insets show the zoom in the first 12 h (a) and 1 h (b). The 0D temperature is not visible in the insets as it is monotonically decreasing in (a) and totally overlapping with the 3D solid line in (b).

1
2
3
4
5
6
7
8
9
10
11
12
13
14
15
16
17
18
19
20
21
22
23
24
25
26
51

The velocity field after 3 days from the initiation of the transient is reported in Fig. 10. The fluid enters the VV from the lower port, as in the upper port region the flow is mainly outwards, see Fig. 10. This behaviour meets the expectations of a natural circulation flow, where the air, heated up by the contact with the hot chamber walls, flows upwards having a lower density. In the bottom region, most of the entering mass flow rate flows towards the IB, since a larger gap between the divertor and VV walls is present with respect to the OB side, see the insets in Fig. 10. This rising mass flow rate of fresh air splits in the several gaps present in the lower part of the chamber, see Fig. 11: the main flow (indicated with “A”) splits in:

- B: rising flow along the gap between the back of the IB segments and the VV walls;
- C: flow in the gap between adjacent divertor cassettes;
- D: flow in the gap between the two IB segments. Note that in Fig. 10 the symmetry plane cuts in half this gap. In addition, since the entering mass flow rate must flow through a much smaller cross-section, it accelerates, as it can be noticed in Fig. 10;
- E: the flow in the gap between the IB segments and the divertor cassettes.

27 Except for “B”, all the other contributions flow
28 towards the plasma chamber. However, most of the fluid
29 rises along the gap rather than flowing inside the plasma
30 chamber (see Fig. 10), as the flow driver is the density
31 (temperature) difference, which is maximum close to the
32 chamber surface; the fluid which enters the plasma
33 chamber slows down and shows some low-velocity
34 vortices. The air flows outside of the plasma chamber
35 inside the upper port region from the gap between the IB
36 and OB segments. At this point, however, the fluid has
37 already heated up significantly (see Fig. 8), so the cooling
38 of the top portion of the BB is less effective. Therefore, if
39 a faster cooling is required than foreseen in Fig. 9, an
40 active cooling system will be needed, which would also
41 allow cooling first the top part of the segment, thus
42 significantly reducing the unavailability; on the other
43 hand, cooling (actively) the BB from the top would be
44 counterposed by the natural convection, so an additional
45 (parametric) analysis is envisaged, to assess how
46 beneficial forced convection could be. Another possible
47 solution, which could be further investigated in the future,
48 is the possibility to cool down the BB segments to a lower
49 temperature than 300 °C prior to disconnecting the
50 primary coolant system.



52
53
54
55

Fig. 10. Velocity magnitude and vector field on the symmetry plane of the maintained sector, 3 days after the beginning of the transient; the insets report the detail of the flow field at the bottom of the IB and OB segments.

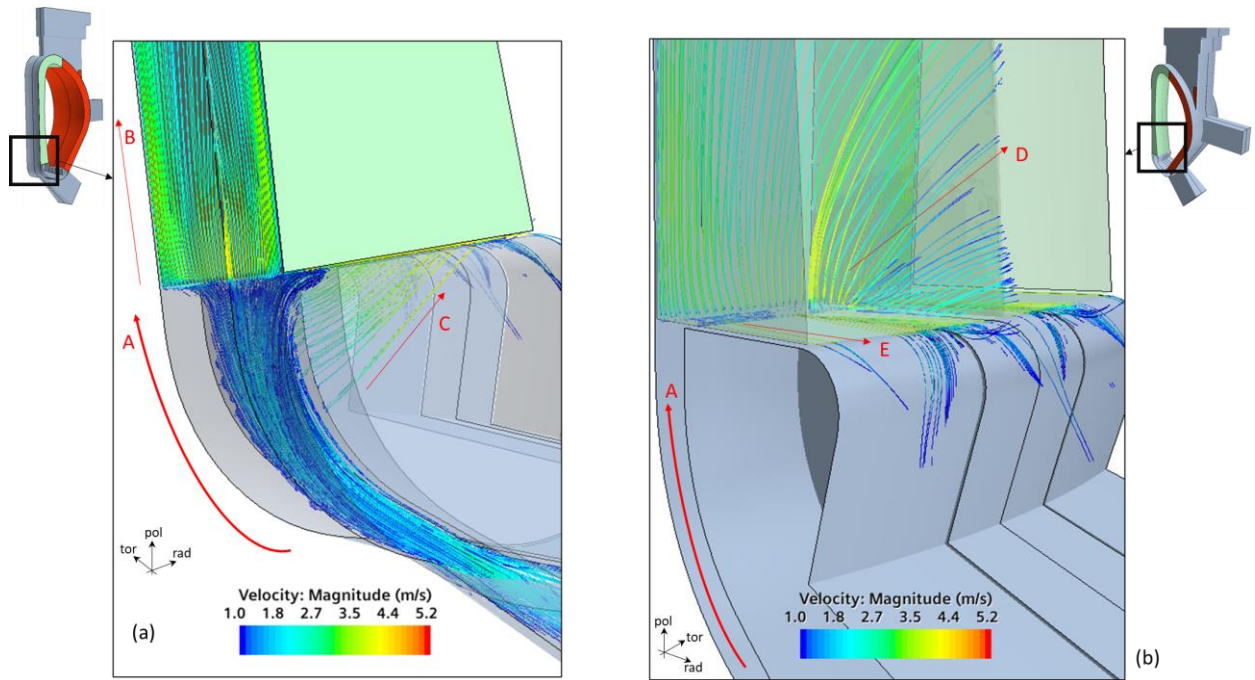


Fig. 11. Streamlines after 9 days from the beginning of the transient in the (a) region between the divertor cassettes and VV walls and in the (b) bottom region of the IB segments and divertor cassettes facing the plasma chamber. A: main flow from the lower port towards IB; B: flow between the back of the IB segments and the VV walls; C: flow between adjacent divertor cassettes; D: flow between adjacent IB segments; E: flow between IB segments and divertor cassettes.

Concerning the (local) heat transfer coefficient HTC_{local}^{comp} , it is computed according to

$$HTC_{local}^{comp} = \frac{q_s''}{(T_s - T_{ref,in})} \quad (10)$$

where q_s'' is the surface heat flux, T_s is the surface temperature and $T_{ref,in}$ is a reference temperature, assumed equal to the inlet temperature.

HTC_{local}^{comp} confirms the behavior discussed above. The fluid travels with larger velocities close to the bottom part of the segments, thus leading to larger heat transfer coefficients in that region, see Fig. 12. On the contrary, the surfaces facing the plasma chamber are characterized by low, i.e. very close to zero, heat transfer coefficient, because the fluid is almost stagnant there. Furthermore, during the transient, the thermal driver becomes less strong (because the segments cool down, thus the temperature difference between the solids and the fluid is smaller), so the average velocity of the fluid is lower. This has an impact on the heat transfer coefficient, which becomes lower and lower throughout the transient, see Fig. 12. Indeed, the average heat transfer coefficient (weighted on the wetted surfaces) is equal to 2.4 W/(m² K) and to 1.8 W/(m² K) after 6 hours and 10 days from the beginning of the transient, respectively. Note that these average values are in line with the rough estimation obtained with available correlations, see Appendix A.

Finally, it is important to highlight that the time computed to reach 150 °C on both IB and OB segments

is, in some sense, conservative, since the radiative heat transfer towards the VV (and, to a lesser extent, divertor) surfaces at low temperatures would help to reduce the BB temperature and has been neglected in this work.

6. Conclusions and perspective

A 3D transient CFD model has been developed to analyse the CHT problem of natural convection cooling of a sector of the HCPB BB in the EU DEMO tokamak, investigating the time needed, starting 1 month after reactor shutdown, to cool down the BB until the RH system requirements are met. A detailed model of the 47 sector under maintenance has been included, with a refined mesh in the small gaps between the BB segments and the VV. All the other sectors have been included, to take into account also the flow of air towards the non-maintained sectors.

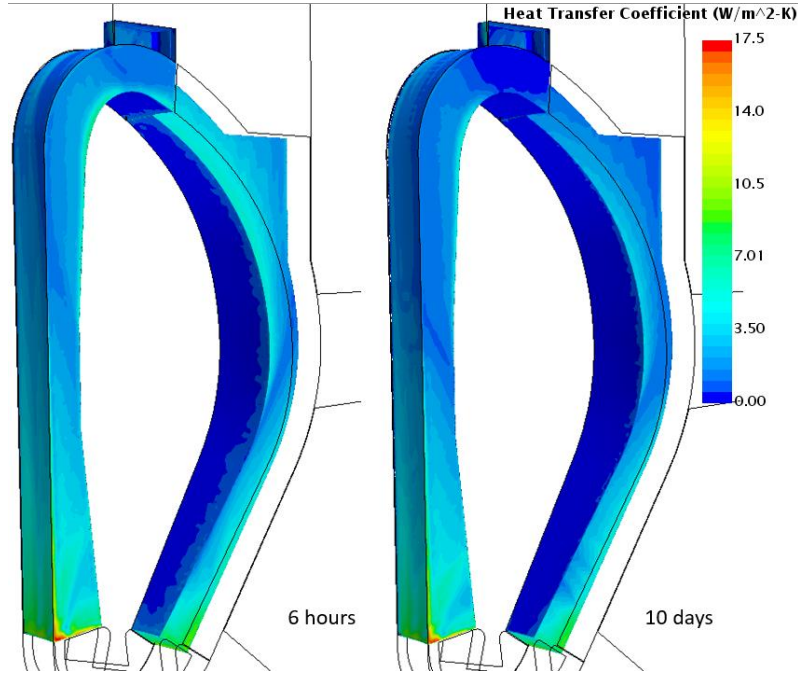
The model results show that, assuming the start of the transient 1 month after the reactor shutdown, ~15 days are needed to cool the top of the OB segments and ~85 days for the IB segments; considering that the OB segments will be removed first, RH operation could, however, start after 15 days.

In perspective, the model will be applied to analyse the effect of an active cooling system intervening from the upper port, which should reduce significantly the time needed to meet the RH requirements by cooling faster (in forced convection) the top region of the BB, where the RH will be attached to handle the segments. Also, the

1 possibility to actively cool down the segments before
 2 starting the transient will be investigated. In addition, it
 3 should be interesting to perform a similar analysis for the

4 Water-Cooled Lithium-Lead BB concept, which, having
 5 a different material composition, may be characterized by
 6 much different time scales.

7



8

9

10 Fig. 12. Distribution of the heat transfer coefficient on the surfaces of one IB and one OB segment after 6 hours and 10 days
 11 from the beginning of the transient.

12

13

14 **Acknowledgements**

15 This work has been carried out within the framework
 16 of the EUROfusion Consortium and has received funding
 17 from the Euratom research and training programme 2014-
 18 2018 and 2019-2020 under grant agreement No. 633053.
 19 The views and opinions expressed herein do not
 20 necessarily reflect those of the European Commission.
 21 The work of A. Froio is financially supported by a
 22 EUROfusion Engineering Grant.

23 Computational resources were provided by
 24 HPC@POLITO, a project of Academic Computing
 25 within the Department of Control and Computer
 26 Engineering at the Politecnico di Torino
 27 (<http://www.hpc.polito.it>).

28

29 **Appendix A. Validation on a simplified case**

30 To check and validate the chosen models and solvers,
 31 as well as the meshing strategy, a simple natural
 32 convection case has been set up, to compare the computed
 33 Nusselt number Nu with that given by available
 34 correlations.

35 A steady-state 2D model has been set up,
 36 characterized by a vertical parallel plate channel,
 37 according to the scheme in Fig. 13; the length of the
 38 channel has been chosen in order to have fully developed

39 flow. In analogy with the case of the BB cooling, a
 40 pressure of 0 Pa gauge and a temperature of 26 °C are
 41 imposed as inlet and outlet boundary conditions, and a
 42 uniform heat flux of 100 W/m² is imposed on the walls.
 43 The resulting value of Ra , computed as

$$Ra = \frac{g\beta q'' \delta^3}{k\nu\alpha} \quad (11)$$

44 since the wall heat flux q'' is imposed [22], is $Ra \cong$
 45 2×10^4 , so the flow will be laminar. All models and
 46 solvers adopted here are the same as those reported in
 47 section 4 above.

48

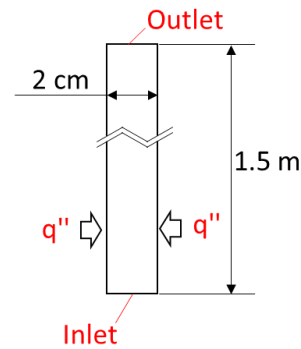


Fig. 13. Sketch of the 2D model used for the validation.

49

50

51

52

1 In the case of fully developed flow, the value of Nu at
 2 channel outlet can be computed according to the
 3 experimental correlation [22]

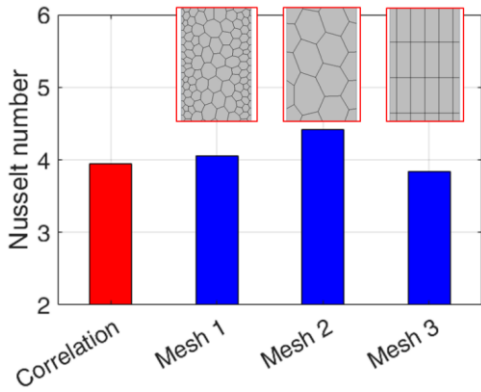
$$Nu = 0.144 \sqrt{Ra \frac{\delta}{L}} \quad (12)$$

4 where L is the length of the channel. The corresponding
 5 heat transfer coefficient, considering as characteristic
 6 length the gap width, is equal to $4 \text{ W}/(\text{m}^2 \text{ K})$.

7 Three different meshes have been adopted, which are
 8 shown in Fig. 14: “Mesh 1” is a fine unstructured
 9 polygonal mesh, and features ~ 10 cells in the channel
 10 width; “Mesh 2” is a coarse unstructured polygonal mesh,
 11 with ~ 4 cells in the channel width; “Mesh 3” is a
 12 structured rectangular mesh with 6 cells in the channel
 13 width. The most suitable meshing strategy for the 3D case
 14 will be chosen comparing this 2D result with correlation
 15 (12).

16 The results are reported in Fig. 14: both Mesh 1 and
 17 Mesh 3 give a Nu value within 3 % from the correlation,
 18 which is nearly 1/3 of the deviation obtained with Mesh
 19 2. Furthermore, a grid independence study on the number
 20 of layers shows that using 6 layers the error on the
 21 computed Nu stays below 3 % with respect to a much
 22 more refined grid (24 layers), thus 6 layers are chosen to
 23 mesh the gap. This suggests that the models and solvers
 24 chosen as well as the meshing strategy for the gaps can be
 25 considered reliable also in the fully 3D problem, which is
 26 the 3D version of Mesh 3 (see Fig. 5c).

27



28 Fig. 14. Comparison of the Nu obtained from the
 29 correlation (12) and numerically, with three different
 30 meshes.
 31
 32

33

34 Appendix B. Material properties

35 In order to simplify the geometry (i.e. to avoid
 36 describing in detail the internals of the BB), the solid
 37 material of the BB segments is assumed homogeneous.
 38 The BB segments contain a mixture of EUROFER97
 39 Reduced-Activation Ferritic-Martensitic steel (structural
 40 material), Li_4SiO_4 pebbles (breeder material), Be_{12}Ti rods
 41
 42

43

41 (neutron multiplier material), W (First Wall armour) and
 42 He (coolant). The volumes of the different materials in the
 43 IB, central OB (COB) and Left/Right OB (LOB/ROB) BB
 44 segments are reported in Table 1.

45 The properties are homogenised in order to conserve
 46 the total heat capacity and diffusivity of each segment; in
 47 addition, since the properties show a variation in the
 48 temperature range of interest ($150\text{--}400 \text{ }^\circ\text{C}$) below 5 %
 49 [21], a constant, average value is assumed for the entire
 50 transient duration. The homogenised values are reported
 51 in Table 2.

52 To conserve the total mass of the solid object M , the
 53 density is a volume-averaged value, according to

$$M = \bar{\rho} V_{tot} = \sum_{i=1}^N \rho_i V_i \Rightarrow \bar{\rho} = \frac{\sum_{i=1}^N \rho_i V_i}{V_{tot}} \quad (13)$$

54 where $\bar{\rho}$ is the average density, $V_{tot} = \sum_{i=1}^N V_i$ is the total
 55 solid volume, $N = 5$ is the number of different materials
 56 in the BB segments, ρ_i is the density of the i -th material,
 57 and V_i is the volume of the i -th material.

58 To conserve the total heat capacity of the solid object
 59 C , the (mass) specific heat is a mass-averaged value,
 60 according to

$$C = M \bar{c} = \sum_{i=1}^N \rho_i c_i V_i \Rightarrow \bar{c} = \frac{\sum_{i=1}^N \rho_i c_i V_i}{M} \quad (14)$$

61 where \bar{c} is the average specific heat and c_i is the specific
 62 heat of the i -th material.

63 To conserve the heat diffusivity of the solid object, the
 64 thermal conductivity is a volume-averaged value,
 65 according to

$$\bar{k} = \frac{\sum_{i=1}^N k_i V_i}{V_{tot}} \quad (15)$$

66 where \bar{k} is the average thermal conductivity and k_i is the
 67 thermal conductivity of the i -th material.

68

69 Table 1. Volume of different materials in the HCPB BB [25].

70

Material	COB	LOB/ROB	IB
EUROFER97	6.53 m ³	6.20 m ³	4.03 m ³
Li_4SiO_4	1.83 m ³	1.74 m ³	1.13 m ³
Be_{12}Ti	6.07 m ³	5.76 m ³	3.75 m ³
W	0.047 m ³	0.044 m ³	0.029 m ³
He	6.38 m ³	6.06 m ³	3.94 m ³

71

72 Appendix C. Space and time convergence studies

73 The choice of the grid size and timestep used in the
 74 work has been undertaken via convergence analyses; the
 75 quantity used for the analyses is the volume-averaged
 76 temperature in the solid domain after 13 ks (i.e. $\sim 3.6 \text{ h}$) of
 77 transient T_{solid}^{ave} .

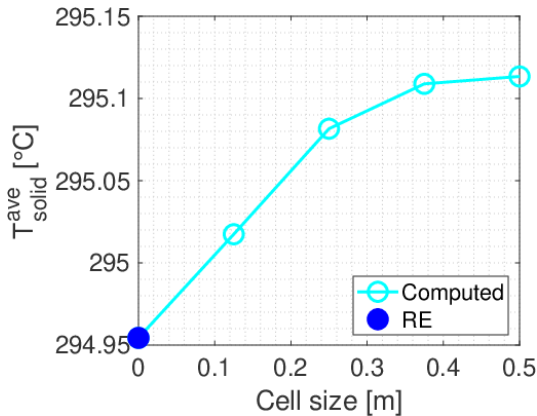
78

Table 2. Material properties in the HCPB BB.

Material	k [W/(m K)]	c [J/(kg K)]	ρ [kg/m ³]
EUROFER97 [21]	25.2	574.0	7685
Li ₄ SiO ₄ [21]	0.920	1789	1526
Be ₁₂ Ti [26]	34.3	2384	3468
W [27]	149	139.0	19290
He [28]	0.249	5190	6.611
Homogenised	18.4	1143	3647

5 Space convergence

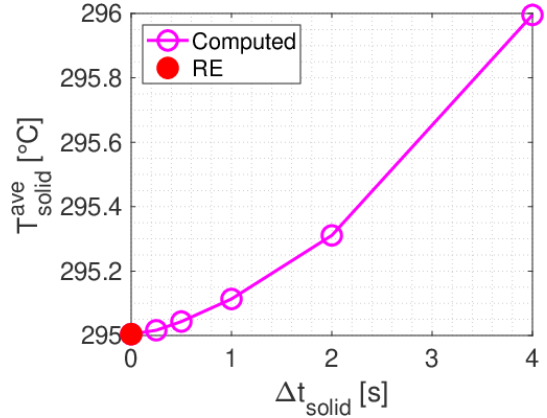
6 Four different meshes are created, having a
 7 characteristic cell size of 0.5 m, 0.375 m, 0.25 m and
 8 0.125 m, corresponding to a total cell count of
 9 ~402 thousands, ~691 thousands, ~1.60 million, and
 10 ~5.83 million, respectively. The values of T_{solid}^{ave} for the
 11 different grids are reported in Fig. 15, together with the
 12 “exact” value estimated with the Richardson
 13 Extrapolation (RE) technique [29] (filled circle). For all
 14 the four grids, the error with respect to the exact value is
 15 <3.2 %, so the coarsest grid is chosen for the analysis



19 Fig. 15. T_{solid}^{ave} for the different grids (empty circles) and
 20 “exact” value estimated with RE.

22 Time convergence

23 Similarly to the space convergence study, five
 24 different time steps for the “solid” physics Δt_{solid} have
 25 been used (0.25 s, 0.5 s, 1 s, 2 s and 4 s), keeping constant
 26 the $\Delta t_{fluid}/\Delta t_{solid}$ ratio (see section 3 above). The
 27 corresponding values of T_{solid}^{ave} are reported in Fig. 16,
 28 together with the “exact” value estimated with the RE
 29 technique (filled circle). For $\Delta t_{solid} = 1$ s, an error of
 30 ~2.2 % is found, which is comparable to (and below) the
 31 value obtained for the space convergence, so 1 s is chosen
 32 as time step for the analysis.



34 Fig. 16. T_{solid}^{ave} for the different time steps (empty
 35 circles) and “exact” value estimated with RE.

39 References

- 40 [1] A. J. H. Donné, W. Morris, X. Litaudon, C. Hidalgo,
 41 D. McDonald, H. Zohm, E. Diegele, A. Möslang,
 42 K. Nordlund, G. Federici, P. Sonato, C. Waldon, D. Borba
 43 and P. Helander, European research roadmap to the
 44 realisation of fusion energy, EUROfusion Consortium,
 45 2018. [Online]. Available: [https://www.euro-](https://www.euro-fusion.org/fileadmin/user_upload/EUROfusion/Document/s/TopLevelRoadmap.pdf)
 46 [fusion.org/fileadmin/user_upload/EUROfusion/Document](https://www.euro-fusion.org/fileadmin/user_upload/EUROfusion/Document/s/TopLevelRoadmap.pdf)
 47 [s/TopLevelRoadmap.pdf](https://www.euro-fusion.org/fileadmin/user_upload/EUROfusion/Document/s/TopLevelRoadmap.pdf). [Accessed 2 June 2020].
 48 [2] F. Cismondi, L. V. Boccaccini, G. Aiello, J. Aubert,
 49 C. Bachmann, T. Barrett, L. Barucca, E. Bubelis,
 50 S. Ciattaglia, A. Del Nevo, E. Diegele, M. Gasparotto,
 51 G. Di Gironimo, P. A. Di Maio, F. A. Hernández,
 52 G. Federici, I. Fernández-Berceruelo, T. Franke, A. Froio,
 53 C. Gliss, J. Keep, A. Loving, E. Martelli, F. Maviglia,
 54 I. Moscato, R. Mozzillo, Y. Poitevin, D. Rapisarda,
 55 L. Savoldi, A. Tarallo, M. Utili, L. Vala, G. Veres and
 56 R. Zanino, Progress in EU Breeding Blanket design and
 57 integration, Fusion Engineering and Design 136(A):782-
 58 792, 2018.
 59 [3] G. A. Spagnuolo, G. Bongiovi, F. Franza and I. A. Maione,
 60 Systems Engineering approach in support to the breeding
 61 blanket design, Fusion Engineering and Design
 62 146(A):31-35, 2019.
 63 [4] G. A. Spagnuolo, L. V. Boccaccini, G. Bongiovi,
 64 F. Cismondi and I. A. Maione, Development of load
 65 specifications for the design of the breeding blanket system,
 66 Fusion Engineering and Design 157:111657, 2020.

- 1 [5] J. Keep, S. Wood, N. Gupta, M. Coleman and A. Loving,
2 Remote handling of DEMO breeder blanket segments:
3 Blanket transporter conceptual studies, Fusion Engineering
4 and Design 124:420-425, 2017.
- 5 [6] Siemens, STAR-CCM+, 2019. [Online]. Available:
6 [https://www.plm.automation.siemens.com/global/it/prod
7 ucts/simcenter/STAR-CCM.html](https://www.plm.automation.siemens.com/global/it/products/simcenter/STAR-CCM.html). [Accessed 27 November
8 2019].
- 9 [7] D. Leichtle, P. Pereslavtsev, J. Sanzi, J. P. Catalan and
10 R. Juarez, Global shutdown dose rate maps for a DEMO
11 conceptual design, Fusion Engineering and Design
12 98-99:1524-1527, 2015.
- 13 [8] Y. Someya, H. Utoh, R. Hiwatari, H. Tanigawa, K. Tobita
14 and the Joint Special Design Team for Fusion, Shutdown
15 dose-rate assessment during the replacement of in-vessel
16 components for a fusion DEMO reactor, Fusion
17 Engineering and Design 124:615-618, 2017.
- 18 [9] B. Končar, M. Draksler, O. Costa Garrido and
19 B. Meszaros, Thermal radiation analysis of DEMO
20 tokamak, Fusion Engineering and Design 124:567-571,
21 2017.
- 22 [10] B. Končar, O. Costa Garrido M. Draksler, R. Brown and
23 M. Coleman, Initial optimization of DEMO fusion reactor
24 thermal shields by thermal analysis of its integrated
25 systems, Fusion Engineering and Design 125:38-49, 2017.
- 26 [11] M. Draksler, B. Končar, M. Tekavčič and C. Bachmann,
27 CFD analysis of the natural circulation of helium in the
28 DEMO cryostat during a leak accident, Fusion
29 Engineering and Design 158:111752, 2020.
- 30 [12] Siemens, STAR-CCM+ User's Manual, v2019.3.
- 31 [13] R. Wenninger, DEMO1 Reference Design – 2017 March
32 ("EU DEMO1 2017"), EFDA_D_2NE9JA, 2017,
33 unpublished.
- 34 [14] C. Gliss, June-2017 DEMO Reference Configuration
35 model, EFDA_D_2N4EZW, 2017, unpublished.
- 36 [15] F. A. Hernández, P. Pereslavtsev, G. Zhou, B. Kiss,
37 Q. Kang, H. Neuberger, V. Chakin, R. Gaisin,
38 P. Vladimirov, L. V. Boccaccini, G. A. Spagnuolo,
39 S. D'Amico and I. Moscato, Advancements in the Helium-
40 Cooled Pebble Bed Breeding Blanket for the EU DEMO:
41 Holistic Design Approach and Lessons Learned, Fusion
42 Science and Technology 75(5):352-364, 2019.
- 43 [16] A. Del Nevo, P. Arena, G. Caruso, P. Chiovaro,
44 P. A. Di Maio, M. Eboli, F. Edemetti, N. Forgiione,
45 R. Forte, A. Froio, F. Giannetti, G. Di Gironimo, K. Jiang,
46 S. Liu, F. Moro, R. Mozzillo, L. Savoldi, A. Tarallo,
47 M. Tarantino, A. Tassone, M. Utili, R. Villari, R. Zanino
48 and E. Martelli, Recent progress in developing a feasible
49 and integrated conceptual design of the WCLL BB in
50 EUROfusion project, Fusion Engineering and Design
51 146(B):1805 1809, 2019.
- 52 [17] F. Cisondi, private communication, 2018.
- 53 [18] S. Irving, B. Fordand and D. Etheridge, Natural
54 ventilation in non-domestic buildings, CIBSE
55 Applications Manual AM10, 2005.
- 56 [19] C. Bachmann and F. Cisondi, private communication,
57 Jan. 2019.
- 58 [20] T. Härtl, C. Bachmann, E. Diegele and G. Federici,
59 Rationale for the selection of the operating temperature of
60 the DEMO Vacuum Vessel, Fusion Engineering and
61 Design 146:1096-1099, 2019.
- 62 [21] P. Frosi, IVC RM interface temperatures during shutdown,
63 EFDA_D_2MAG8P, 2018, unpublished.
- 64 [22] F. Incropera and D. Dewitt, Fundamentals of heat and
65 mass transfer, 7th edition, John Wiley & Sons, 2011.
- 66 [23] STAR-CCM+ User's Manual v14.06.
- 67 [24] [dataset] A. Zappatore and A. Froio, CFD analysis of
68 natural convection cooling of the in-vessel components
69 during a shutdown of the EU DEMO fusion reactor
70 (dataset), Zenodo, v1.0.0, 2020, [10.5281/zenodo.3922265](https://doi.org/10.5281/zenodo.3922265).
- 71 [25] F. A. Hernández, P. Pereslavtsev, G. Zhou, Q. Kang,
72 S. D'Amico, A. Retheesh and H. Neuburger, HCPB
73 design and integration studies 2019, EFDA_D_2NKC7G,
74 2020, unpublished.
- 75 [26] M. Uchida, E. Ishizuka and H. Kawamura, Thermal
76 conductivity of neutron irradiated Be₁₂Ti, Fusion
77 Engineering and Design 69(1-4):499-503, 2003.
- 78 [27] M. Fukuda, A. Hasegawa and S. Nogami, Thermal
79 properties of pure tungsten and its alloys for fusion
80 applications, Fusion Engineering and Design 132:1-6,
81 2018.
- 82 [28] E. W. Lemmon, M. L. Huber and M. O. McLinden,
83 Reference Fluid Thermodynamic and Transport Properties,
84 NIST Standard Reference Database 23, version 9.1, 2013.
- 85 [29] P. J. Roache, Verification and validation in computational
86 science and engineering; Hermosa Publishers,
87 Albuquerque, NM, USA, 1998.
- 88